

The electrochemical lithium reactions of monoclinic ZnP_2 material†‡

Haesuk Hwang,^a Min Gyu Kim,^b Youngsik Kim,^c Steve W. Martin^c and Jaephil Cho^{*a}

Received 20th February 2007, Accepted 4th April 2007

First published as an Advance Article on the web 24th April 2007

DOI: 10.1039/b702648j

Monoclinic ZnP_2 particles were synthesized by vacuum annealing of a mixture consisting of P and Zn powders at 1000 °C. In contrast to a tetragonal Zn_3P_2 phase, a very large plateau corresponding to 1000 mAh g⁻¹ at ~0.45 V was developed, and out to 545 mAh g⁻¹, only topotactic lithium ion intercalation into the molecule pores was observed. The excess Li ion uptake beyond simple Li intercalation (>545 mAh g⁻¹) into molecular pores can break a chemical bond between Zn and the phosphorus atoms. During discharge, the formation of the Li_nP clusters (LiP_5 and LiP) and Zn, LiZnP phases were dominant as a result of the local structural distortion around the ZnP_4 tetrahedral site. During charge, Zn and LiP_5 phases transformed into ZnP_2 and LiP phases. However, decomposition reactions of the LiP and ZnP_2 phases with the electrolyte led to the capacity fade of the cell.

Introduction

Zn metal can react with 1.5 moles of Li, thus forming the $\text{Li}_{1.5}\text{Zn}$ alloy, but the capacity of the Zn in ZnM is reported to be strongly dependent on the metal (M). Zn_3N_2 exhibits a large reduction capacity of 1325 mAh g⁻¹ corresponding to 3.7 Li per Zn, but only 555 mAh g⁻¹ is reversible.¹ The reaction mechanism is a conversion reaction of Zn_3N_2 into LiZn and a matrix phase of $\beta\text{-Li}_3\text{N}$, the high pressure form of Li_3N . On the other hand, Zn_4Sb_3 shows first discharge and charge capacities of ~680 mAh g⁻¹ and ~507 mAh g⁻¹, respectively.² *Ex situ* XRD patterns of the Zn_4Sb_3 electrode show several lithium-containing compounds such as LiZbSb , Li_3Sb , and LiZn .

Recently, Bichat *et al.* prepared the $\alpha\text{-Zn}_3\text{P}_2$ phase by using ball milling and the first and second discharge capacities were 995 mAh g⁻¹ and 666 mAh g⁻¹, respectively, showing a rather fast capacity fade.³ Based upon results of *ex situ* XRD patterns, they proposed that Zn_3P_2 had two distinct parallel reversible pathways for a large number of inserted lithiums. The first involves exclusively phosphide phases such as Zn_3P_2 , LiZnP , Li_4ZnP_2 , and Li_3P . The second one involves only the Li–Zn alloys of Zn, LiZn_4 , and LiZn .

Similar MP anodes have been intensively investigated and as of yet, an MP that maintains its original structure after full lithium alloying (down to 0 V) is rare. MP anodes undergo phase separation depending on the nature of the metal in the metal phosphides and their composition and structure.^{3–7}

CoP_3 ,^{8,9} NiP_2 ,¹⁰ VP_4 ,¹¹ Sn_4P_3 ,¹² and $\text{GaP}^{13,14}$ are observed phase separations when they are discharged to 0 V, thus forming Li_xP phases, while FeP_2 ¹⁵ and CuP_2 ¹⁶ show different behavior to the others, forming a metastable Li–Fe–P phase or Li_2CuP phase. In the case of MnP_4 ,¹⁷ topotactically inserted Li_7MnP_4 is decomposed to Li_3P and Mn nanoparticles below 0.5 V. Recently, some studies on ternary Li–M–P systems (Li_xMnP_4) have shown a reversible ordered–disordered phase transformation accompanied by structural arrangements during lithium alloying/dealloying.^{17–20} For instance, Li_xTiP_4 ternary phases ($x = 7$ and 9) show Li_9TiP_4 , leading to a specific capacity of 970 mAh g⁻¹ without showing decomposition reaction.¹⁸ However, in the case of $\text{SnP}_{0.94}$, Li ions are inserted/extracted via a reaction of $\text{SnP}_{0.94} + 4.5 \text{ Li} \leftrightarrow \text{Li}_{4.5}\text{SnP}_{0.94}$ without destroying Sn and P bonding.²¹

In this study, we report lithium reactions of monoclinic ZnP_2 prepared by solid state reaction in a vacuum-sealed quartz tube using P and Zn metals during electrochemical lithium alloying and dealloying between 2 and 0 V.

Experimental

In order to synthesize ZnP_2 material, the surface moisture on the inner surface of the quartz tube was removed using a gas torch. When the residual moisture was present in the quartz tube, it reacted with P during the thermal annealing process partially forming P_2O_5 . A stopcock assembly utilizing a rubber hose and hose clamp was attached to the tube, and a vacuum was pulled through a liquid N_2 trap. Heat was then applied to the tube using a gas torch, and the surface moisture on the quartz tube was driven off. The closed tube was then transferred to the glove box. In order to prepare monoclinic ZnP_2 , 1.53 g of Zn metal (99.9%, Aldrich) and 1.75 g of red phosphorus (99.999%, Aldrich) was charged into the quartz tube with a stop cock. Finally, the tube was evacuated utilizing a vacuum pump and a nitrogen trap using a gas torch. The tube was placed in a vertical furnace and maintained at 1000 °C for 5 h, cooled to 700 °C and maintained for 3 h, followed by quenching at room temperature.

^aDepartment of Applied Chemistry, Kumoh National Institute of Technology, Gumi, Korea 730-701. E-mail: jpcho@kumoh.ac.kr

^bBeamline Research Division, Pohang Accelerator Laboratory, Pohang, Korea 790-784

^cDepartment of Materials Science & Engineering, Iowa State University, Ames, IA 50010, USA

† This paper is part of a *Journal of Materials Chemistry* theme issue on New Energy Materials. Guest editor: M. Saiful Islam.

‡ Electronic supplementary information (ESI) available: Fig. S1: Plots of voltage curves of Zn electrode between 2 and 0 V and *ex situ* XRD patterns of the Zn electrode after 0 V discharge and 2 V charge; Fig. S2: SEM images of the Zn electrode before and after first cycling. See DOI: 10.1039/b702648j

The electrode composition used was ZnP_2 : PvDF binder : carbon black in a weight ratio of 8 : 1 : 1. The electrolyte used was 1 M LiPF_6 with ethylene carbonate/diethylene carbonate/ethyl methyl carbonate (vol% = 3 : 3 : 4 (EC/DEC/EMC)). Lithium metal was used as a counter electrode. The cycle life of the cells was tested between 2 V and 0 V at a rate of 0.1 C. For the *ex situ* XRD measurement, the cells charged or discharged to certain voltages were disassembled in a glove box and the electrodes were rinsed thoroughly with a DMC solution to remove the LiPF_6 salts. XRD patterns were obtained using a $\text{Cu K}\alpha$ X-source on a Rigaku instrument operated at 11 kW.

Electrochemical *in situ* cell preparation for extended X-ray absorption fine structure (EXAFS) and X-ray absorption near edge structure (XANES) measurements was carried out in an inert gas filled glovebox to prevent any oxidation and contamination. After being assembled with Li foil, a separator, and a $\sim 40\ \mu\text{m}$ thick ZnP_2 electrode ($25 \times 25\ \text{mm}$), the cell was vacuum sealed with an aluminium pouch. The X-ray photon flux was enough to transmit through the electrochemical cell without any chemical interaction. Zn K-edge X-ray absorption spectra were recorded on the BL7C1 beam line of a Pohang light source (PLS) with a ring current of 140–190 mA at 2.5 GeV. A Si(111) double crystal monochromator was employed to monochromatize the X-ray photon energy. The data were collected in transmission mode with N_2 gas filled ionization chambers as detectors. Higher order harmonic contaminations were eliminated by detuning to reduce the incident X-ray intensity by $\sim 30\%$. Energy calibration was simultaneously carried out for each measurement with Zn foil placed in front of the third ion chamber. The data reduction of the experimental spectra was performed by the standard procedure reported previously.¹³ Total *in situ* XAFS spectra were divided into two voltage regions, discharging–charging to 0.0–2.0 V with a current of 4.0 mA and 0.45–2.0 V with a current of 3.0 mA.

Results and discussion

Fig. 1 shows the XRD pattern of as-prepared ZnP_2 which can be indexed to a monoclinic phase with a space group $C/2m$. The lattice constants a and c were estimated to be 8.864(1) Å and 7.571(0) Å, respectively. Fig. 2a exhibits an SEM image of the as-prepared ZnP_2 particle, consisting of stacked layers, and

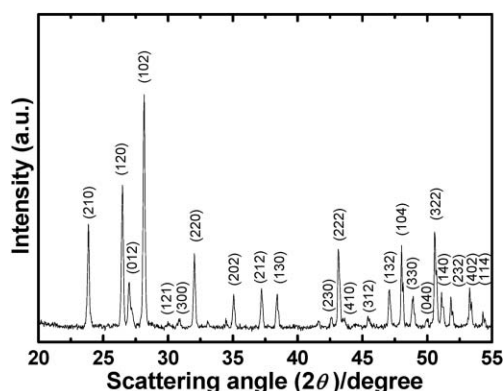


Fig. 1 Powder XRD pattern of the as-prepared ZnP_2 particles.

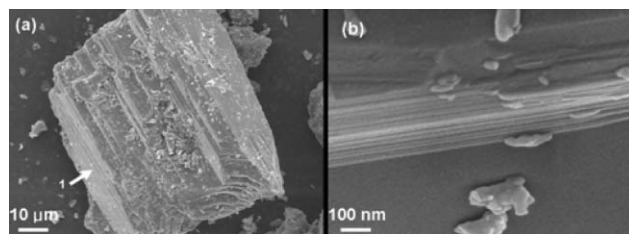


Fig. 2 SEM images of (a) as-prepared ZnP_2 particles and (b) expanded image of the arrowed part in (a).

an expanded image along the direction marked 1 in Fig. 2a, showing that the interlayer distance was $\sim 10\ \text{nm}$, is shown in Fig. 2b. Fig. 3 shows voltage profiles of the ZnP_2 between 2 and 0 V at a rate of 0.1 C ($=150\ \text{mA g}^{-1}$). The first discharge and charge capacities of the ZnP_2 were $1,490\ \text{mAh g}^{-1}$ and $910\ \text{mAh g}^{-1}$, respectively. However, while the irreversible capacity ratio of the ZnP_2 anode is 40%, it exhibits rapid capacity fading, having 30% capacity retention after only 3 cycles. At $\sim 0.45\ \text{V}$, a wide range of the plateau is developed out to $1100\ \text{mAh g}^{-1}$.

Fig. 4 shows selected *ex situ* XRD patterns obtained at different discharging and charging states from Fig. 3 (points 1 to 10). Down to point 3, which corresponds to $545\ \text{mAh g}^{-1}$ ($\text{Li}_{2.6}\text{ZnP}_2$), new peaks do not develop, indicating topotactic Li insertion into the monoclinic structure. 2.6 Mole of Li in $\text{Li}_{2.6}\text{ZnP}_2$ was calculated from electrochemical data ($545\ \text{mAh g}^{-1}$) based upon assumptions that other side reactions did not occur, such as (1) capacity contribution from possible SEI film, (2) a small amount of new phase (Zn or LiP_5) that could be invisible in the XRD pattern, (3) simultaneous process of the Li insertion into the monoclinic structure and the decomposition of the monoclinic phase due to local differences in the electrode such as particle sizes and polarization status. In addition, major peaks slightly shift to lower angles, indicating a small volume expansion during the lithium intercalation. When the discharge capacity reaches $653\ \text{mAh g}^{-1}$ (point 4), the $\text{Li}_{2.6}\text{ZnP}_2$ phase starts to decompose to Zn and LiP_5 phases. Further lithium reaction to point 5 results in $875\ \text{mAh g}^{-1}$, and the decomposition of the

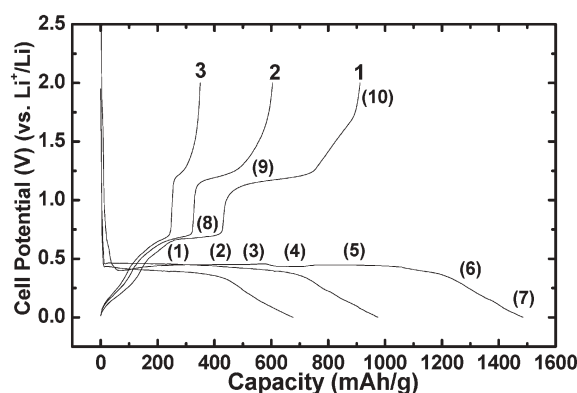


Fig. 3 Voltage curves of the first discharge and charge process between 2 and 0 V at a rate of 0.1 C using a coin-type half cell. The numbers denoted on the curves indicate the points at which *ex situ* XRD patterns of the ZnP_2 electrodes were taken.

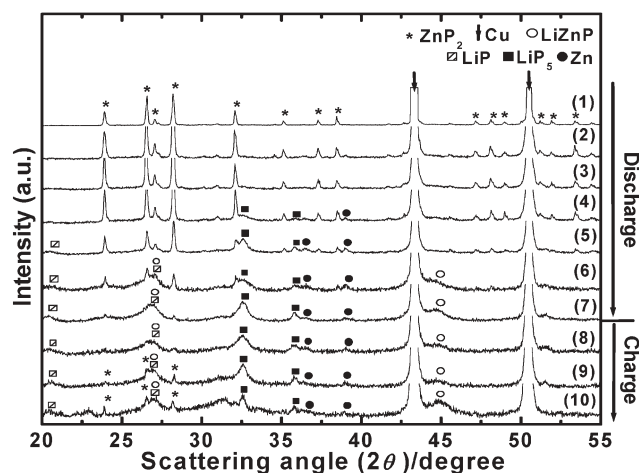


Fig. 4 Ex situ XRD patterns of the ZnP_2 electrode using points in Fig. 3.

$\text{Li}_{2.6}\text{ZnP}_2$ phase accelerates, growing the LiP_5 , Zn , and LiP phases. Simultaneously, the LiZnP phase starts to grow at point 6. At zero voltage (point 7), the monoclinic Li_xZnP_2 phase almost disappears, and mixed phases consisting of LiP , LiP_5 , Zn , and LiZnP phases are predominant. Tetragonal $\alpha\text{-Zn}_3\text{P}_2$ exhibited the formation of the Li-Zn alloys such as LiZn_4 , Li_2Zn_5 , and LiZn ,³ but monoclinic ZnP_2 did not show such phases.

During charge (points 8 to 10), LiP_5 , LiP , LiZnP , and Zn phases similar to those observed during the discharge process were also observed, but the XRD peak intensities of LiP_5 and Zn phases decrease, compared with points 7 and 8 during discharge. In the case of tetragonal Zn_3P_2 , the conversion of LiZnP into Li_4ZnP_2 under lithiation at ~ 0.5 V results in a strong peak at $\sim 42^\circ$ corresponding to the Li_4ZnP_2 phase.³ However, in our case, the phase transition to Li_4ZnP_2 did not occur. On the other hand, we can note that the intensity of the monoclinic ZnP_2 phase increased up to 2 V (point 10), which may be due to the possible reaction of LiP_5 and Zn phases according to: $\text{LiP}_5 + 2\text{Zn} \rightarrow 2\text{ZnP}_2 + \text{P}$. Further, during charging (dealloying), the decreasing intensity of LiP_5 and concurrent increasing intensity of the LiP phase indicate the progressive phase transition from LiP_5 to LiP . In addition, from the XRD pattern at point 10, the increased peak intensity of the LiZnP phase is noticeable, compared with that at point 9.

Fig. 5 shows a differential capacity plot as a function of the potential between the first and third cycles, and peaks at ~ 0.43 V, ~ 0.67 V and ~ 1.17 V during discharge and charge, respectively, were observed in cycles one, two, and three. We can observe that the peak intensities of the peaks at ~ 0.43 V, ~ 0.67 V and ~ 1.17 V decrease rapidly upon cycling. This result indicates that rapid capacity fading of the ZnP_2 may be related to such rapidly decreased peak intensities. XRD patterns of the discharged ZnP_2 electrode at ~ 0.43 V after first and third cycles show the decreased peak intensities of $\text{Li}_{2.6}\text{ZnP}_2$, LiP_5 and LiZnP phases, compared with those after 1 cycle (Fig. 6a). This result indicates that the instability of the $\text{Li}_{2.6}\text{ZnP}_2$, LiP_5 , and LiZnP phases contributes to the capacity fade. In the XRD pattern at point 8 (~ 0.67 V), compared with

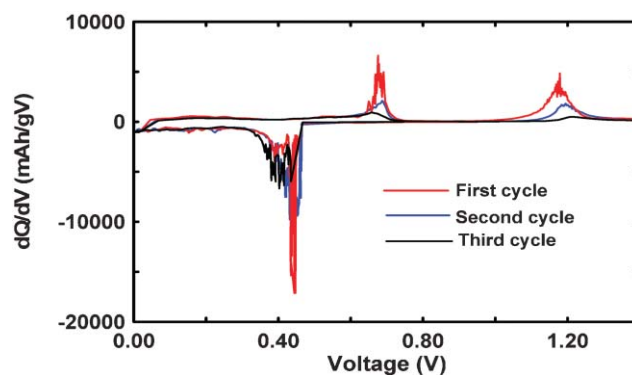


Fig. 5 Differential capacity plots as a function of potential between the first and third cycles using the cycling curves in Fig. 3.

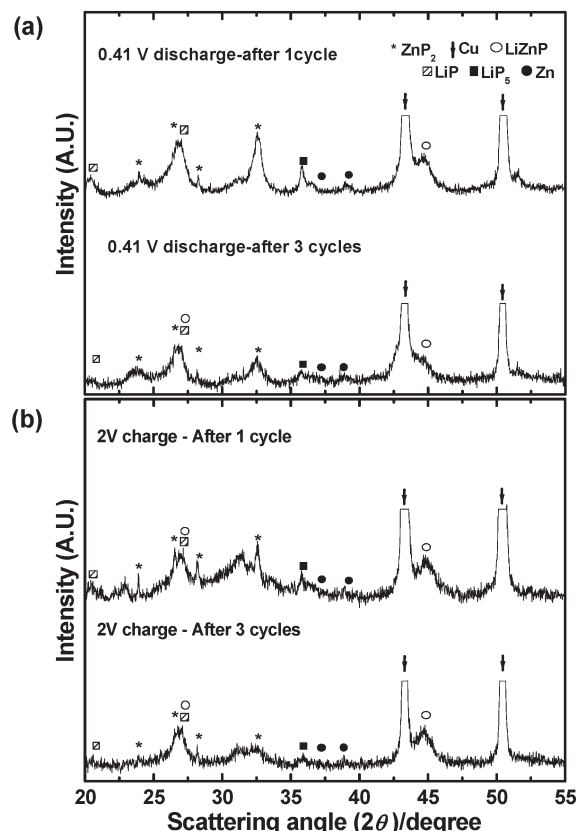


Fig. 6 XRD patterns of (a) the discharged and (b) the charged ZnP_2 electrodes to 0.41 V and 2 V after the first and third cycles, respectively.

that at point 7, decreasing peak intensities of Zn and LiP_5 are dominant, indicating the possible phase transformed reaction of $\text{LiP}_5 + 2\text{Zn} \rightarrow 2\text{ZnP}_2 + \text{P}$. At point 9 (~ 1.17 V), we can observe increased peak intensities of LiP and ZnP_2 phases, and therefore we can propose the following decomposition reaction without removing the lithium from LiP_5 , LiP_5 (173 mAh g^{-1}) + $2\text{Zn} \rightarrow \text{LiP}$ (864 mAh g^{-1}) + 2ZnP_2 , where LiP and ZnP_2 are formed at the expense of the LiP_5 and Zn phases. From these reactions, the peak at ~ 0.67 V corresponds to the phase transition from LiP_5 and Zn to the ZnP_2 phase, and the peak at ~ 1.17 V corresponds to the phase

transition from LiP_5 and Zn to LiP. From these results, we can conclude that the reactions of ZnP_2 and LiP phases are major contributors for the capacity fade of the cell. Actually, the XRD patterns of the charged electrode after 3 cycles (Fig. 6b) clearly show the decreasing intensities of the ZnP_2 and LiP phases, compared with the intensities after the first cycle, supporting the differential capacity result. After the first cycling, we examined the SEM images of the electrode (Fig. 7), and the initial morphology appears to have completely disappeared, and particles were severely aggregated and cracked. It has been reported that the most prevalent reasons for capacity fade in the metal alloys are 1) electrical disconnection of the electrode from the current collector caused by the compositional volume changes occurring during cycling, and as the particles fragment, they become electrically isolated, which reduces the cell capacity and 2) onset of the side reactions due to a slight instability of the phosphorus-based reaction products with the present electrolytes, leading to some decomposition.⁹ Presently, the second reason is much more likely to account for capacity loss in the metal phosphides because microstructure control did not affect the capacity enhancement.²² Accordingly, electrolyte decomposition reactions catalyzed by ZnP_2 and LiP decomposition may enhance the cracking and crumbling of the electrode during cycling, resulting in a continuous generation of new active surfaces that were previously passivated by the stable surface films. Hence, the repeated reaction between the electrolyte and the electrode materials induces capacity fading.

In addition, in order to see the capacity fade contribution of Zn metal, the coin-type half cell containing Zn metal was cycled between 0 and 2 V (see ESI†): the initial discharge capacity and charge capacity were 410 and 196 mAh g^{-1} , respectively, and it showed much improved capacity retention upon cycling, compared to ZnP_2 . Fig. 8 shows XRD patterns of Zn metal after full discharge to 0 V and charging to 2 V to investigate the alloy formation with Zn. At 0 V, Li_2Zn_5 , LiZn_2 , and LiZn_4 phases occur, and subsequent charging to 2 V leads to increasing intensity of Zn metal while the intensities of the LiZn_2 and LiZn_4 phases decrease. However, Li_2Zn_5 seems to retain its intensity even after fully charging. This indicates that once Li_2Zn_5 forms, it does not undergo further reaction with Li. Instead, LiZn_2 decomposed to $2\text{Zn} + \text{Li}$. SEM images of the cycled Zn electrode showed that the initial particle morphology before cycling is sustained after cycling, indicating that Zn and phase do not influence the capacity loss (see ESI†).

In situ Zn K-edge XAFS experiments were carried out in order to confirm the structural evolution of ZnP_2 during Li reactions. Fig. 8 shows the spectral variation of cut-off

voltage-resolved Zn K-edge XANES spectra and the corresponding Fourier transform (FT) magnitudes of the EXAFS spectra for the first cycle in the voltage regions between 2.0 and 0.0 V. The monoclinic ZnP_2 consists of a molecular channel hybridized by both zigzagging and honeycomb-pore structures through a ZnP_4 tetrahedral polymeric network, which can act as a Li intercalating path.

The pristine ZnP_2 has a symmetric FT peak at $\sim 1.9 \text{ \AA}$, corresponding to Zn–P bonding. The first electrochemical Li ion uptakes show no effective spectral change for the electrochemical reaction, meaning that Li ion uptake into molecular pores with appropriate free volume is possible without molecular structural change of ZnP_2 . Higher Li ion insertion after scan 8 begins to result in a local structural variation of the ZnP_2 molecular pore. The FT peak intensity of Zn–P bonding becomes weak and another FT peak is newly generated at about 2.2 \AA , indicating the occurrence of Zn–Zn metallic bonding. The peak intensity of Zn–P rapidly decreases but that of Zn–Zn rapidly increases in the following Li ion insertions. The overall FT peak features are constant until discharging to 0.0 V (scan 16), which gives spectral evidence for perfect phase transition from the zinc phosphide form to the Zn metallic phase. The excess Li ion uptakes beyond simple Li intercalation into molecular pores can break chemical bonds between Zn and the phosphorus atoms. The formation of the Li_nP clusters is followed by local structural distortion

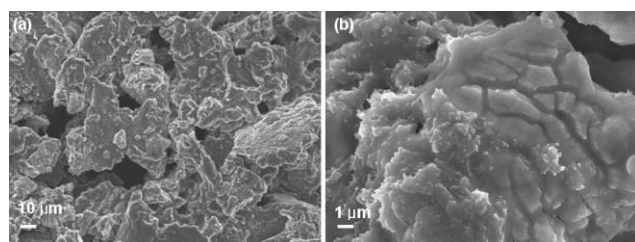


Fig. 7 SEM images of the ZnP_2 electrode after the first cycle.

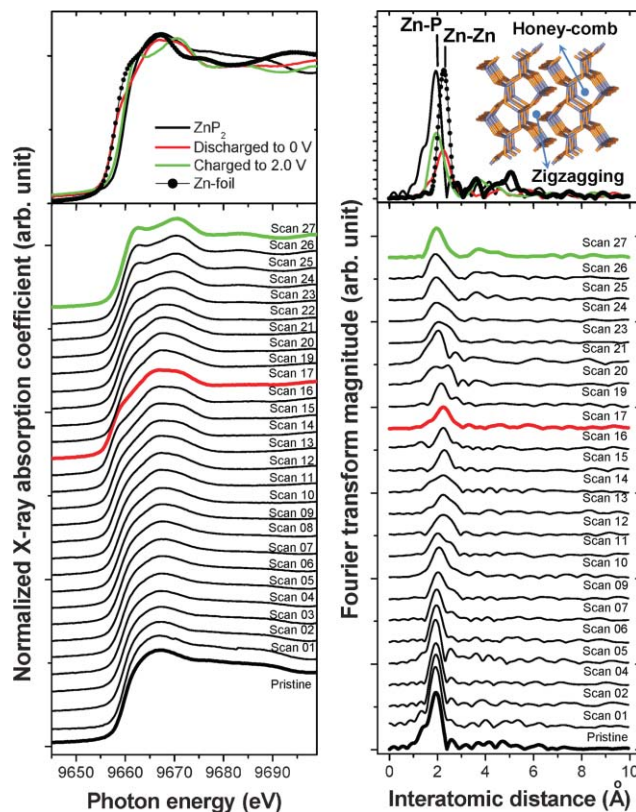


Fig. 8 Spectral variation of *in situ* Zn K-edge XANES spectra (left) and Fourier transform (FT) magnitudes for EXAFS spectra (right) in the voltage region between 2.0 and 0.0 V during the first cycling. The inset shows possible Li-ion uptakes into molecular channels viewed down the $\langle 001 \rangle$ direction.

around the ZnP_4 tetrahedral site. Consecutive Li ion uptakes lead to atomic rearrangement of free Zn atoms, and subsequently to the formation of a Zn metallic phase. The weak FT peak intensity of scan 16 with respect to that of reference Zn metal means that the Zn metallic phase formed in the higher lithiated region cannot grow up to the bulk scale. The existence of neighboring Li_nP clusters is believed to prevent the Zn metallic clusters from aggregating. As a result, the overall electrochemical Li ion uptake behavior for molecular pore ZnP_2 leads to the phase transition to the Zn metallic phase *via* Li ion intercalation through molecular pores, which can be supported with peak feature variation of the XANES spectra.

Upon charging, the FT peak feature gradually shifts to the lower r space region of 1.9 Å for Zn–P chemical bonding. Only pure Zn–P chemical bonding is observed in charging to 2.0 V, although the FT peak intensity rapidly decreases and is relatively broad with respect to that of the pristine ZnP_2 . The spectral recovery into the overall FT characteristics for the Zn–P phase indicates the structural variation of ZnP_2 is reversible for the first cycle, namely inter-conversion between Zn phosphides and Zn metallic phase. For the GaP system reported earlier,¹³ on the other hand, aggregated Ga metallic clusters in the fully discharged state cannot be pulverized to form chemical bonds with phosphorus atoms on charging. This is due to the existence of the Li_nP matrix which prevents reversible formation of chemical bonds between Ga and phosphorus atoms. The structural difference in the charging process can be explained from the viewpoint of the molecular structures of the pristine sample. While the crystal structure of GaP has only honeycomb pores, the ZnP_2 shows another pore structure of zigzagging channels, as shown in the inset of Fig. 8. Therefore, it can be deduced that the reversible return of the Zn–P phase is possible from another phosphorus source in the lattice.

In order to explore the possibility of only Li intercalation occurring into the molecular channel of the ZnP_2 , *in situ* XAFS characterization was carried out for the first and second cycles in the voltage region between 2.0 and ~0.45 V which corresponds to ~545 mAh g⁻¹ (Fig. 9). For the first cycling up to 0.0 V, the molecular pore ZnP_2 phase could be used as two kinds of anode materials. Namely, the phase could potentially be used as a Li ion intercalating system into molecular channels in the intermediate voltage region and a phase transition system into Zn alloying until 0.0 V. In the voltage region before the transition to the metallic phase, it can be anticipated that ZnP_2 is utilized only as a pure Li ion intercalating anode into molecular channels. Fig. 9 shows Zn K-edge XANES and FT of EXAFS spectral variation in the voltage region. Upon totally discharging, all FT peak features are constant at 1.9 Å with Zn–P chemical bonding. No FT peak shift to the higher r space region is observed, indicating that no Zn–Zn metallic bonding occurs. The charging to 2.0 V after the first cycle also shows the constant FT peak feature, as well as the reversible return of XANES spectra. The second cycling also presents similar peak characteristics to the first cycling. The spectral results suggest that the Li ion uptakes can be intercalated into molecular channels until ~545 mAh g⁻¹ without structural cleavage of monoclinic ZnP_2 . This means that the hybridized zigzagging and honeycomb pore structures

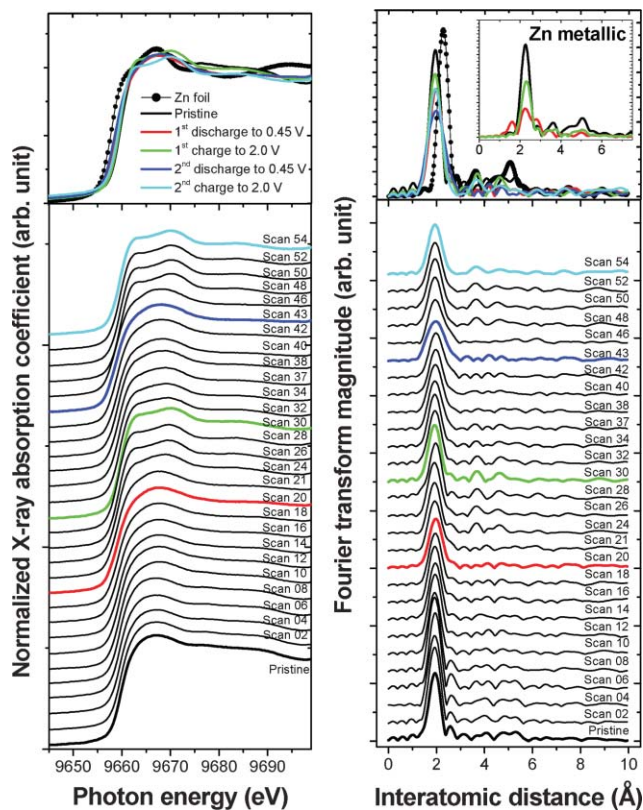


Fig. 9 Spectral variation of *in situ* Zn K-edge XANES spectra (left) and Fourier transform (FT) magnitudes for EXAFS spectra (right) in the voltage region between 2.0 and 0.45 V during the first and second cycles. The inset shows FT peak features of discharging to 0.0 V and charging to 2.0 V for the reference Zn metallic powder.

allow the structural stabilization of the discharge capacity without a phase transition. Therefore, ZnP_2 material has the potential to be applied in parallel as two kinds of anode materials, the phase transition to Zn alloying until 0.0 V *via* Li ion intercalating, as well as the only Li ion intercalating system into molecular channels in the voltage region up to 0.45 V. This result is consistent with XRD patterns of the ZnP_2 electrode cycled between 2 and 0.45 V, as shown in Fig. 10. In this voltage range, although first discharge and charge capacities of the electrode were 540 and 440 mAh g⁻¹, respectively, the initial ZnP_2 phase is maintained without transforming into other phases.

Overall, lithium reaction mechanisms can be summarized based upon XRD and XAS results. Fig. 11 shows a schematic description summarising the phase transitions occurring on discharge and on charge. During the discharge process, topotactic lithium ion intercalation into the pore structures of ZnP_2 to $\text{Li}_{2.67}\text{ZnP}_2$ occurs at first, and the gradual decomposition of $\text{Li}_{2.67}\text{ZnP}_2$ to LiP, LiP₅, Zn, and LiZnP phases follows. Hence, we can estimate the discharge capacity at 0 V as the following reaction: 2LiP_5 (346 mAh g⁻¹) + LiZnP (278 mAh g⁻¹) + LiP (864 mAh g⁻¹) + Zn. The estimated capacity is 1488 mAh g⁻¹, which agrees well with the actual discharge capacity of 1490 mAh g⁻¹. During the charge, ZnP_2 and LiP phases start to be dominant at the expense of LiP₅ and Zn phases.

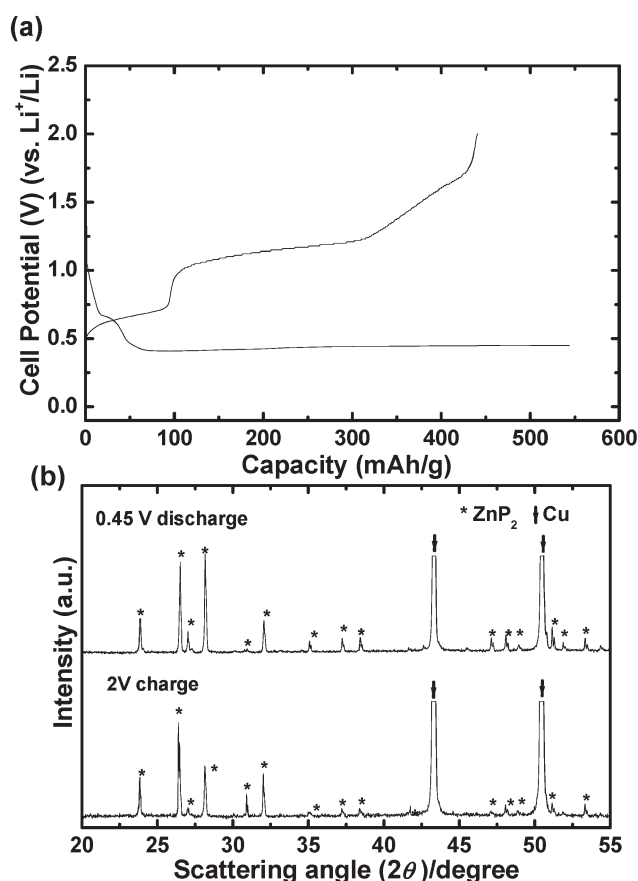


Fig. 10 Plots of (a) voltage curves of ZnP₂ electrode between 0.45 and 2 V, and (b) *ex situ* XRD patterns of the ZnP₂ electrode after 0.45 V discharge and 2 V charge.

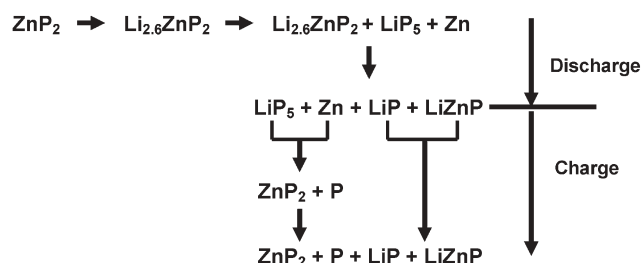


Fig. 11 Schemes that summarize the reactions occurring on discharge and on charge.

Conclusions

Electrochemical Li reaction of the ZnP₂ anode led to first discharge and charge capacities of 1500 mAh g⁻¹ and 910 mAh g⁻¹, respectively, between 0 and 2 V. However, further cycling led to fast capacity fading, and the decomposition reaction of the ZnP₂ and LiP₅ phases with the electrolyte during cycling was believed to play a major role in decreasing the capacity. On the other hand, when the electrochemical window was limited between 2 and 0.45 V in which the lithium

ions intercalated into the pore channels of the monoclinic lattice, the initial ZnP₂ phase was maintained without showing bond breaking between phosphorus and Zn atoms. However, it is essential to see the cyclability out to dozens of cycles for a potential anode material for rechargeable batteries. However, only the first cycle result shows clear evidence for structural stability within a limited voltage window. Currently, extensive cycling tests are under way to examine the relationship between the voltage window and structural stability.

Acknowledgements

The authors wish to acknowledge the Pohang Light Source (PLS) for the XAS measurements. This research was financially supported by the Ministry of Commerce, Industry and Energy (MOCIE) and Korea Industrial Technology Foundation (KOTEF) through the Human Resource Training Project for Regional Innovation.

References

- 1 N. Pereira, L. C. Klein and G. G. Amatucci, *J. Electrochem. Soc.*, 2002, **149**, A262.
- 2 X. B. Zhao and G. S. Cao, *Electrochim. Acta*, 2001, **46**, 891.
- 3 M. P. Bichat, J.-L. Pascal, F. Gillot and F. Favier, *Chem. Mater.*, 2005, **17**, 6761.
- 4 H. Pfeiffer, F. Tancrét and T. Brousse, *Electrochim. Acta*, 2005, **50**, 4763.
- 5 M. P. Bichat, T. Politova, J. L. Pascal, F. Favier and L. Monconduit, *J. Electrochem. Soc.*, 2004, **151**, A2074.
- 6 H. Pfeiffer, F. Tancrét, M.-P. Bichat, L. Monconduit, F. Favier and T. Brousse, *Electrochem. Commun.*, 2004, **6**, 263.
- 7 S. Woo, J.-H. Jung, H. Kim, M. G. Kim, C. K. Lee, H.-J. Sohn and B. W. Cho, *J. Electrochem. Soc.*, 2006, **153**, A1979.
- 8 V. Pralong, D. C. S. Souza, K. T. Leung and L. F. Nazar, *Electrochem. Commun.*, 2002, **4**, 516.
- 9 R. Alcantara, J. L. Tirado, J. C. Jumas, L. Monconduit and J. Olivier-Fourcade, *J. Power Sources*, 2002, **109**, 308.
- 10 F. Gillot, S. Boyanov, L. Dupont, M. Doublet, M. Moncrette, L. Monconduit and J.-M. Tarascon, *Chem. Mater.*, 2005, **17**, 6327.
- 11 Y.-U. Kim, B. W. Cho and H.-J. Sohn, *J. Electrochem. Soc.*, 2005, **152**, A1475.
- 12 Y.-U. Kim, C. K. Lee, H.-J. Sohn and T. Kang, *J. Electrochem. Soc.*, 2004, **151**, A933.
- 13 H. Hwang, M. G. Kim and J. Cho, *J. Phys. Chem. C*, 2007, **111**, 1186.
- 14 M. V. V. M. S. Kishore and U. V. Varadaraju, *J. Power Sources*, 2005, **156**, 594.
- 15 D. C. C. Silva, O. Crosnier, G. Ouvrard, J. Greedan, A. Safa-Sefat and L. F. Nazar, *Electrochem. Solid-State Lett.*, 2003, **6**, A162.
- 16 K. Wang, J. Yang, J. Xie, B. Wang and Z. Wen, *Electrochem. Commun.*, 2003, **5**, 480.
- 17 D. C. S. Souza, V. Pralong, A. J. Jacobson and I. F. Nazar, *Science*, 2002, **296**, 1012.
- 18 F. Gillot, M. P. Bichat, F. Favier, M. Morcrette, M. L. Doublet and L. Monconduit, *Electrochim. Acta*, 2004, **49**, 2325.
- 19 F. Gillot, L. Monconduit, M. Morcrette, M.-L. Doublet, L. Dupont and J.-M. Tarascon, *Chem. Mater.*, 2005, **17**, 3627.
- 20 O. Cronier, C. Mounsey, P. S. Herle, N. Talyer and L. F. Nazar, *Chem. Mater.*, 2003, **15**, 4890.
- 21 Y. Kim, H. Hwang, M. G. Kim, C. S. Yoon and J. Cho, *Adv. Mater.*, 2007, **19**, 92.
- 22 O. Crosnier and L. F. Nazar, *Electrochem. Solid-State Lett.*, 2004, **7**, 187.